PCCP

Rotational spectroscopy of methyl tert-butyl ether with a new K_a band chirped-pulse Fourier transform microwave spectrometer

Journal:	*Physical Chemistry Chemical Physics*
Manuscript ID	CP-ART-02-2024-000797.R1
Article Type:	Paper
Date Submitted by the Author:	09-Apr-2024

Complete List of Authors:	Crabtree, Kyle; University of California Davis, Department of Chemistry Westerfield, John; University of California Davis, Department of Chemistry Dim, Chisom; University of California Davis, Department of Chemistry Meyer, Kelly; University of California Davis, Department of Chemistry Johansen, Sommer; University of California Davis, Department of Chemistry Buchanan, Zachary; University of California Davis, Department of Chemistry Stucky, Paul; University of California Davis, Department of Chemistry

Journal Name

ARTICLE TYPE

Cite this: DOI: 00.0000/xxxxxxxxxx

Rotational spectroscopy of methyl *tert*-butyl ether with a new K_a band chirped-pulse Fourier transform microwave spectrometer†

Kyle N. Crabtree,*[a] J. H. Westerfield,[b] Chisom A. Dim,[b] Kelly S. Meyer,[b] Sommer L. Johansen,‡[b], Zachary S. Buchanan, [b] and Paul A. Stucky[b]

Received Date
Accepted Date

DOI: 00.0000/xxxxxxxxxx

Chirped-pulse Fourier transform microwave (CP-FTMW) spectroscopy is a powerful tool for performing broadband gas-phase rotational spectroscopy, and its applications include discovery of new molecules, complex mixture analysis, and exploration of fundamental molecular physics. Here we report the development of a new K_a band (26.5–40 GHz) CP-FTMW spectrometer that is equipped with a pulsed supersonic expansion source and a heated reservoir for low-volatility samples. The spectrometer is built around a 150 W traveling wave tube amplifier and has an instantaneous bandwidth that covers the entire K_a band spectral range. To test the performance of the spectrometer, the rotational spectrum of methyl *tert*-butyl ether (MTBE), a former gasoline additive and environmental pollutant, has been measured for the first time in this spectral range. Over 1000 spectroscopic transitions have been measured and assigned to the vibrational ground state and a newly-identified torsionally excited state; all transitions were fit using the XIAM program to a root-mean-square deviation of 22 kHz. The spectrum displays internal rotation splitting, nominally forbidden transitions, and an intriguing axis-switching effect between the ground and torsionally excited state that is a consequence of MTBE's extreme near-prolate nature. Finally, the sensitivity of the spectrometer enabled detection of all singly-substituted ^{13}C and ^{18}O isotopologues in natural abundance. This set of isotopic spectra allowed for a partial r_0 structure involving the heavy atoms to be derived, resolving a structural discrepancy in the literature between previous microwave and electron diffraction measurements.

1 Introduction

Since its development in the mid 2000s, chirped-pulse (CP) spectroscopy in the microwave and millimeter wave has become a widely-used technique for investigating the rotational spectra of small molecules.[1] The exquisite sensitivity of rotational spectroscopy to three-dimensional molecular geometry makes it a powerful tool for determining precise structural parameters of gas-phase molecules. In addition, the intrinsically narrow Doppler widths achievable at low frequency allows for resolution of small splittings arising from large-amplitude motion and intramolecular interactions.[2–8] CP techniques are routinely used to study systems of fundamental interest such as clusters,[9–12] radicals,[13] and astrochemically-relevant species,[14] often in conjunction with a high-resolution, narrow-bandwidth cavity FTMW spectrometer in the centimeter band. In such investigations, the CP spectrum of the system of interest is directly compared against a predicted spectrum from quantum chemical calculations to yield a quick initial fit of experimental spectroscopic constants, followed by targeted measurements with a cavity instrument to explore small splittings as needed. However, the broadband nature of CP spectroscopy coupled with the intrinsically narrow linewidths of rotational spectra are amenable for applications which involve complex mixtures and/or reaction dynamics.[15–21]

The K_a band (26.5–40 GHz) is an attractive spectral region for CP spectroscopy for both fundamental and analytical applications. Compared with lower-frequency instruments that operate in the 2–8, 8–18, or 18–26 GHz regions, the K_a band offers more raw bandwidth and has comparable availability of broadband microwave electronics (e.g., amplifiers, mixers). In addition, the higher frequency range allows for probing a broader range of quantum numbers, thereby enabling determination of more ac-

[a] *Department of Chemistry, University of California, Davis, Davis, CA, United States. Tel: +1 530 752 6024; E-mail: kncrabtree@ucdavis.edu*
[b] *Department of Chemistry, University of California, Davis, Davis, CA, United States.*

† Electronic Supplementary Information (ESI) available: Spectrometer schematic, parts list, and timing diagram; Cartesian coordinates for equilibrium geometries and internal rotation calculations; calculated internal rotation parameters; raw experimental free induction decays; processed spectra; spectroscopic fitting files; A-reduction spectroscopic parameters. See DOI: 00.0000/00000000.

‡ Present Address: Sandia National Laboratories, Livermore, CA, United States.

curate and predictive spectroscopic parameters than is possible at lower frequency, as well as measuring low-J transitions from lighter species. Most critically for CP spectroscopy, pulsed broadband high-power amplifiers (>10 W/GHz) are readily available in this region, unlike at higher frequencies.

To date, only three K_a band CP spectrometers have been reported in the literature. The first[22] employed a 60 W traveling wave tube amplifier (TWTA) and covered the full 26.5 – 40 GHz bandwidth instantaneously. Its chirp was generated by a 3–10.5 GHz microwave signal mixed with a 23 GHz local oscillator (LO) to reach 12.5–20 GHz, then doubled to reach 25–40 GHz. The molecular free induction decay (FID) was downconverted to the 4–19 GHz range with a 44 GHz LO; however intermodulation sidebands were observed arising from strong FID beat signals in the receiver system. A second K_a band system was constructed using a similar 40 W TWTA with an 8 GHz bandwidth; the ∼26–33.5 and ∼33.5–40 GHz chunks of the spectrum are folded by use of a 33.5 GHz LO. The third system uses a 50 W solid-state amplifier in place of a TWTA and operates in two modes: a full-bandwidth mode using upconversion of a 1–14.5 GHz chirp and homoodyne downconversion at 41 GHz, and a second mode with 2 GHz bandwidth that operates at high repetition rate with a fast digitizer.

Here we report the design and construction of a new 150 W K_a band CP-FTMW spectrometer, which to our knowledge is the highest-power, full bandwidth instrument operating in this frequency range. The performance of the spectrometer is demonstrated by recording the jet-cooled spectrum of methyl *tert*-butyl ether (MTBE, $CH_3OC(CH_3)_3$). MTBE is an additive used to raise the octane rating of gasoline, but concerns about its toxicity and its presence in domestic water supplies have led to a ban on its use in the United States and other countries, as well as research on routes toward environmental remediation.[23–25] From the standpoint of rotational spectroscopy, MTBE is an intriguing molecule owing to its extreme near-prolate nature ($\kappa = -0.998$) and the presence of multiple potential sources of internal rotation from the methoxy group and the *tert*-butyl group. To date, only 32 lines in the 9–18.6 GHz region of its rotational spectrum have been measured;[26] based on the observed splittings a barrier height of 498.2±1.7 cm^{-1} was derived for the OCH_3 rotation. No internal rotation splitting arising from either *tert*-butyl rotation or rotation of the *tert*-butyl methyl groups was observed. In addition, spectra of all unique ^{13}C and ^{18}O isotopologues were measured and an experimental structure was derived from a Kraitchmann analysis. However, the C-C bond lengths in the *tert*-butyl group differ by ∼30 mÅ from values from both quantum chemical calculations[27] and electron diffraction measurements.[28,29]

In the K_a band spectroscopy reported here, we increase the number of observed lines to 704 in the ground vibrational state, derive a complete set of quartic centrifugal distortion constants, and a partial set of sextic distortion terms. We have also detected and assigned 407 lines arising from the first torsionally excited state of the OCH_3 rotor, which displays an unusual inversion of the b and c inertial axes with respect to the ground state. In addition, we have measured new transitions arising from all singly-substituted heavy atom isotopologues of MTBE, deriving an improved ground-state r_0 structure that resolves the discrepancy between the previous microwave structure and electron diffraction measurements.

2 Methods

2.1 Rotational Spectroscopy

The block diagram of the new K_a-band CP-FTMW spectrometer is shown in Figure 1. A more detailed schematic and a parts list are available in the ESI. A linear frequency-swept chirped pulse covering 1.52–4.895 GHz is generated by an arbitrary waveform generator (Tektronix AWG70002A) at a sampling rate of 16 GSa/s. The chirp is sent through a low-pass filter (6 GHz, K&L Microwave 6L250-6000/T18000-O/O) and mixed (Marki MWave T3H-18IS) with an 11.52 GHz local oscillator (LO). The LO is generated by one output of a dual-channel frequency synthesizer (Valon Technology 5009) at 5.76 GHz, doubled (Wright Technologies ASX13-220), and bandpass-filtered at 11.52 GHz (K&L Microwave 6C52-11520/T200-O/O). A pair of filters (6 GHz high-pass, Mini-Circuits VHF-6010+, and 10.2 GHz low-pass, K&L Microwave 8L250-10200/T30000-O/OP) is used to select the lower sideband of the mixer output, which now spans 6.625–10 GHz and is reversed with respect to the input chirp. The 6.625–10 GHz chirp is then amplified (Miteq AFSD5-060120-30-26P) and converted to 26.5–40 GHz with a frequency quadrupler (Wright Technologies ASX40-420). Following a final pair of filters (26.5 GHz high-pass, AMTI H26G40G1, and 43 GHz low-pass, Marki MWave FLP-4300) and a programmable step attenuator (Agilent 84907L), the chirp is amplified to high power with a TWTA (Applied Systems Engineering 187Ka-H). To balance the chirp flatness and power, the step attenuator is set to 20 dB; the resultant measured output power varies from a minimum of 49.6 dBm at 40 GHz to a maximum of 53.1 dBm at 38 GHz when driving a dummy 50Ω load; from 28-39 GHz the output power is roughly constant at 52–53 dBm before dropping to 50.7 dBm at 26.5 GHz.

The TWTA output is coupled through WR-28 waveguide through a Kapton window into a 25 dBi horn antenna (Advanced Technical Materials PNR 28-449-6/24) which is mounted inside an Eccosorb-lined ISO-400 6-way cross vacuum chamber equipped with a diffusion pump (Varian VHS-400). A second 25 dBi horn is located 33 cm away to receive the molecular free-induction decay (FID). The signal is transferred to coaxial cable and sent through a DC block (Tektronix PSPL5509), a diode limiter (Clear Microwave LT1840H), and a fast PIN diode switch (Quinstar QSC-ASR000) which remains open during the chirped pulse excitation and closed while recording the molecular FID. It is then amplified with a low-noise amplifier (Miteq AMF-6F-26004000-25-13P, noise figure 2.5 dB) and downconverted (Marki MWave ML1-1644IS) at 40.96 GHz. The downconversion LO is generated by the second output of the same dual-channel synthesizer used for the upconversion LO; it begins at 5.12 GHz before being octupled (Wright Technologies APS15-0191) and sent through a bandpass filter (41±0.3 GHz, Eastern Wireless EWT-31-0351). A final 17.4 GHz low-pass filter (Marki MWave FLP-1740) selects the lower sideband of the mixer output, and the resultant 0.96–14.46 GHz signal is amplified (Mini-

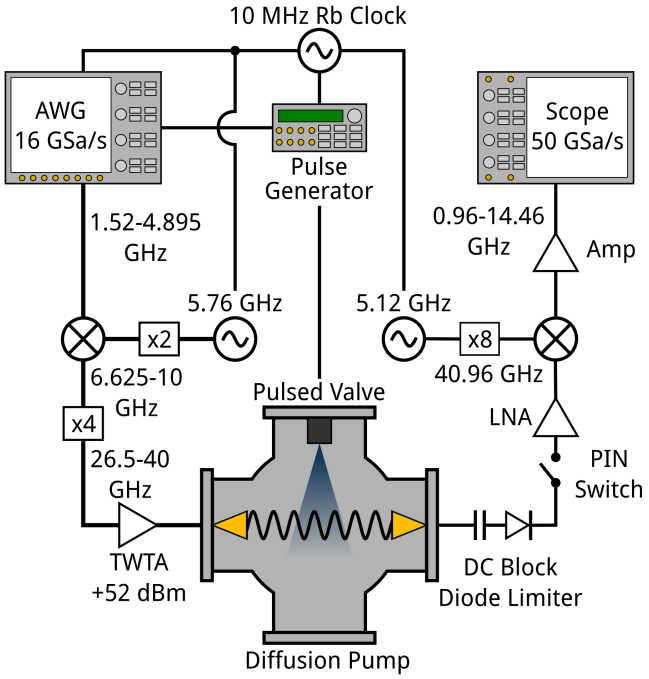

Fig. 1 Simplified block diagram of the K_a band spectrometer. A more detailed schematic is available in the ESI.

circuits ZVA-183-S+) and digitized at 50 GSa/s by an oscilloscope (Tektronix DSA71604C) with 16 GHz analog bandwidth. All microwave sources are referenced to a 10 MHz signal generated by a Rb clock (Stanford Research Systems FS725); however the oscilloscope uses its own internal reference. Connecting the oscilloscope to the external 10 MHz reference yields spurious signals throughout the entire spectrum.

The base repetition rate of the experiment is controlled by a Stanford Research Systems DG645 delay generator which is referenced to the Rb clock. Its output is used to trigger the arbitrary waveform generator as well as a Quantum Composers 9528 digital pulse generator, which in turn controls the timing of pulses sent to a Parker Series 9 solenoid valve via an Iota One pulse driver to generate a supersonic expansion. This approach using two delay generators was found to mitigate timing jitter (and hence phase incoherence) introduced in the process of driving the valve. The general valve is outfitted with a 0.5 mm diameter pinhole and is secured into a plate mounted 22 cm upstream of the horn antennas. In addition, an optional heated reservoir made from an adapted Swagelok inline particulate filter assembly (SS-4F-05) may be placed directly before the general valve. When operated in this configuration, the reservoir and valve are wrapped with 20 Ω heating tape and aluminum foil. A variable AC transformer is used to apply current, and the temperature is monitored with a thermocouple that is pressed against the exterior of the reservoir.

Each gas pulse is probed by a series of twenty 3 μs chirps spaced by 20 μs each and the signal is digitized for 15 μs. The acquisition begins prior to the chirp; leakage through the PIN diode switch is sufficient to permit observation of the chirp itself, which is useful for ensuring phase coherence during a long acquisition. Using the FastFrame technology on the scope, the 20 chirp/FID signals may be viewed individually or coaveraged. This particular excitation scheme was found to maximize the number of chirps that could be fit into the ~500 μs gas pulse while maintaining an intensity of at least 50% relative to the peak molecular signal while monitoring frames individually. During an experiment, the 20 frames are coaveraged on the oscilloscope and transferred to a computer for further time-domain averaging. With this scheme, the maximal data averaging rate is 100 FIDs/sec at a gas pulse rate of 5 Hz, limited by the time required to coaverage the 20 frames on the oscilloscope. Further increase of the gas repetition rate up to 25 Hz is possible without loss of molecular signal; however, the number of chirps per pulse must be decreased in order to avoid missing trigger events while the oscilloscope is processing data. An increase of at least a factor of 5 in acquisition rate would be possible with an improved fast digitizer.

Three total sets of experimental conditions were used for the spectroscopy shown here. For the first two, MTBE was placed into a bubbler which was immersed in a bath of room-temperature water and its vapor entrained in a flow of Argon at 3.75 bar (775860 FIDs, 2h 10m integration time) and 1.0 bar (525660 FIDs, 1h 30m) pressure, respectively. For each of these experiments, a teflon "cap" was placed onto the end of the general valve faceplate; the cap has a 5 mm diameter, 11 mm long inner bore. Gas exiting the pinhole in the faceplate initially expands into the bore, then undergoes a secondary expansion into the vacuum chamber. Empirically we have found that this configuration suppresses the formation of Ar van der Waals clusters while still achieving a rotational temperature of 5–10 K at a 3.75 bar backing pressure. Initial analysis of the MTBE ground vibrational state and the ^{13}C isotopologues was performed with the 3.75 bar Ar spectrum, and final analysis of the ground and vibrationally excited states used the 1.0 bar Ar spectrum, which resulted in a warmer temperature. The FIDs were zero-padded to a length of 2^{20} samples and the initial 4.45 μs of the 15 μs record (containing the chirp) was zeroed out, yielding an effective FID duration of 10.55 μs. A Hanning window function was applied prior to the Fourier transform.

The 3.75 bar Ar spectrum did not achieve sufficient signal-to-noise ratio (SNR) to afford detection of the ^{18}O isotopologue in natural abundance. To further improve the signal level, the Teflon cap was removed and the carrier gas switched for Neon at 3.75 bar. Initial scans showed a much lower temperature, but not an improved signal in the 26.5–40 GHz region. Instead, a few mL of MTBE were adsorbed onto cotton and placed into the heated reservoir; this assembly was then heated to 50°C with 3.75 bar Ne carrier gas. These conditions increased the signal level by a factor of ~2 while keeping a comparable rotational temperature to the 3.75 bar Ar spectrum. However, the sample was exhausted in less than 30 minutes, so this experiment was repeated a total of 7 times to collect 1100940 FIDs (3h total integration time). These FIDs were averaged in the time domain by post-processing, and a phase correction based on the autocorrelation of the chirp was applied, followed by an 7.0 μs exponential filter and a Hanning window. This Ne spectrum was used for the final analysis of all isotopologues.

Spectroscopic analysis was carried out using a modified version of the XIAM$_{mod}$ program.[30] The function of the program remains unchanged; two program files were modified to adjust the display of the intensities in the simulation output and the line errors printed in the fitting output. For the intensities, the original program printed total intensity as a floating point number with 4 decimal places; the modified version prints intensities in scientific notation to handle intensities below 0.0001. The line errors were similarly adjusted to increase the number of digits displayed. Determination of r_0 structures by least-squares fitting was performed with the STRFIT program.[31] Visualizations of molecular structures and calculation of internal rotation parameters were carried out with the moments.py program v4.1.0.[32]

2.2 Calculations

Previous work has shown that MTBE has a C_s equilibrium structure.[27] Accordingly, the structure of MTBE was first optimized with Møller-Plesset second-order perturbation theory (MP2) using the correlation-consistent polarized valence double zeta (cc-pVDZ) basis set[33] using a development version of CFOUR[34] with the constraint of C_s symmetry. The self-consistent field convergence criterion was set to 10^{-10}, and the geometry convergence criterion was a root-mean square force below 10^{-10} Hartree/bohr. This geometry was used as the starting point for harmonic frequency calculations and subsequent anharmonic vibrational calculations using second-order vibrational perturbation theory[35,36] (VPT2) to obtain vibration-rotation interaction parameters and centrifugal distortion constants. A similar calculation was performed using the NASA Ames atomic natural orbital basis set ANO0;[37] owing to the greater computational expense, however, only a smaller subset of force constants sufficient for vibration-rotation analysis were calculated. Following analysis of the spectrum, a VPT2 calculation was carried out at the B3LYP/6-311+G(2d,p) level of theory using Gaussian16[38] for further analysis of centrifugal distortion constants and vibration-rotation interaction parameters. A final pair of geometry optimizations were then performed at the coupled cluster singles, doubles, and perturbative triples [CCSD(T)] level of theory[39,40] with the cc-pVTZ basis set[33] for more accurate structural parameters and to measure the internal rotation barrier height for the methoxy methyl group.

To explore internal rotation motions, a series of potential energy scans were carried out at the MP2/cc-pVDZ and MP2/ANO0 levels of theory using CFOUR interfaced with GeomeTRIC.[41] The three motions investigated in detail were the methoxy methyl rotation (OCH_3), the *tert*-butyl rotation [$C(CH_3)_3$], and the in-plane *tert*-butyl methyl group rotation (CCH_3). For each motion, a relaxed one-dimensional scan was performed by stepping the angle in 10° steps over a range of 180° owing to the overall C_s symmetry, while all other coordinates were optimized. In addition a two-dimensional scan over the OCH_3 and $C(CH_3)_3$ angles was performed: the $C(CH_3)_3$ angle was varied over a 180° range in steps of 10° while the OCH_3 angle was varied over a 350° range, also in steps of 10 °, while all other coordinates were optimized. This calculation was performed only at MP2/cc-pVDZ.

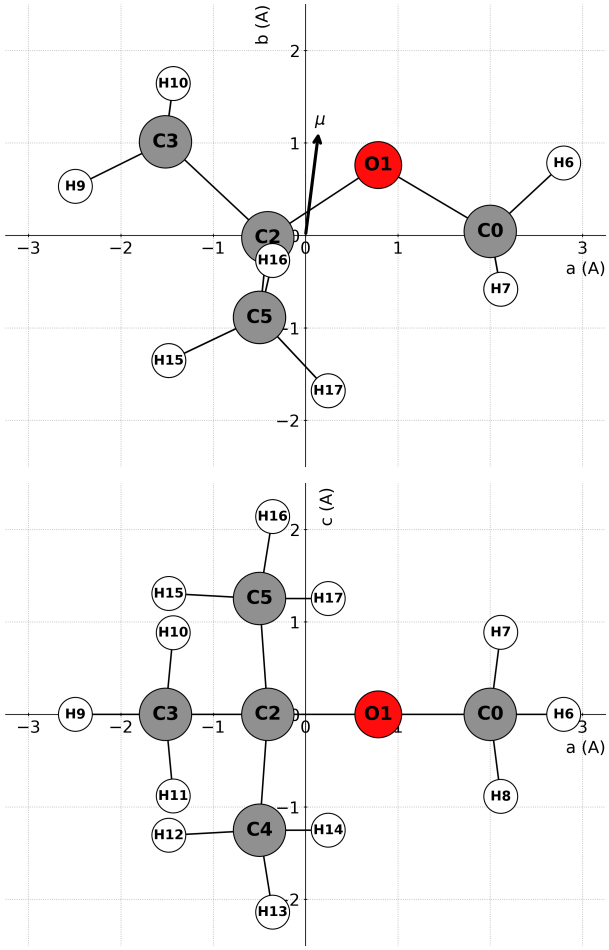

Fig. 2 CCSD(T)/cc-pVTZ structure of MTBE in the *ab* (top) and *ac* (bottom) principal planes.

3 Results

3.1 Calculated Structure

The CCSD(T)/cc-pVTZ structure of MTBE and the atom labeling conventions used here are shown in Figure 2. Bond lengths and angles involving the heavy atoms for the MP2/cc-pVDZ and CCSD(T)/cc-pVTZ calculations are collected in Table 1 and compared with previous MP2 and B3LYP calculations with the DZ+(2p,d) basis set.[27] The present MP2/cc-pVDZ calculations are consistent with the previous ones; bond lengths agree within 5 mÅ and angles within 0.2°. At the CCSD(T) level, the heavy atom bond lengths are all shorter, and most notably, for the *tert*-butyl C−C distances shorten from MP2 to CCSD(T). This trend is opposite compared with MP2 and B3LYP, which saw the C−C bond lengths increase with the higher level of correlation treatment. Here, the C−C bonds are shorter by 15 mÅ compared with the B3LYP geometry. Full sets of Cartesian coordinates are provided in the ESI.

MTBE has a peculiar structure from the perspective of rotational spectroscopy. The rotational constants determined from the calculated structures are shown in Table 2. At the equilibrium geometry, B_e and C_e are nearly equal and the molecule is an extremely near-prolate asymmetric top: $\kappa = -0.991, -0.990,$

Param.	MP2/DZ+(2d,p)[27]	B3LYP/DZ+(2d,p)[27]	MP2/cc-pVDZ	CCSD(T)/cc-pVTZ
$R(C_0O_1)$	1.419	1.412	1.414	1.409
$R(O_1C_2)$	1.440	1.442	1.438	1.432
$R(C_2C_3)$	1.526	1.533	1.527	1.518
$R(C_2C_4)$	1.532	1.539	1.532	1.524
$\angle(C_0O_1C_2)$	116.2	118.0	116.1	116.1
$\angle(O_1C_2C_3)$	103.3	103.5	103.0	103.6
$\angle(C_3C_2C_5)$	110.1	110.1	110.1	110.1

Table 1 Calculated heavy-atom equilibrium (r_e) structural parameters of MTBE. Bond lengths in Å, angles in degrees.

and −0.994 for the MP2/cc-pVDZ, MP2/ANO0, and CCSD(T)/cc-pVTZ structures, respectively. Moreover, because B and C are so close in magnitude, a slight perturbation to the structure can swap the definitions of the inertial axes, causing the O atom (and hence the nonzero dipole moment projection) to lie along the c axis instead of the b axis. While it is fairly common that isotopic substitution may cause a large change in the inertial axis orientation, MTBE is unusual because the vibrational corrections to the rotational constants may be sufficient to swap the axes. As shown in Table 2, the calculated MP2/cc-pVDZ $\Delta B \equiv B_0 - B_e$ value is 10.4 MHz greater in magnitude than ΔC which exceeds the difference in the equilibrium constants, effectively reversing the definitions of the b and c inertial axes in the ground vibrational state. At MP2/ANO0, the difference in ΔB and ΔC is 5.62 MHz and it is further reduced to 1.98 MHz at B3LYP/6-311+G(2d,p). Application of ΔB corrections from either MP2 method to the CCSD(T)/cc-pVTZ equilibrium constants results in reversed inertial axis definitions; however, the B3LYP corrections do not and will therefore be used in later sections. This reversal is not observed in the experimental ground-state rotational spectrum, which displays clear b-type A/E doublets each accompanied by a single forbidden c-type E transition.[26] Even small errors in the rotational constants and vibrational corrections can result in qualitative differences in the spectroscopic predictions so close to the prolate limit.

Calculated normal modes and harmonic frequencies associated with the torsional motions of MTBE are shown in Table 3, along with frequencies derived from gas-phase measurements.[42] These are the five lowest-frequency modes in the molecule. The rest of the harmonic frequencies are provided in the ESI (including values at MP2/ANO0 and B3LYP/6-311+G(2d,p)). In Table 3 the normal modes are described in terms of the torsional dihedral angles: the *tert*-butyl angle $\tau_t \equiv \tau(C_3C_2O_1C_0)$, the methoxy angle $\tau_m \equiv \tau(H_6C_0O_1C_2)$, the in-plane CCH_3 angle $\tau_{ip} \equiv \tau(H_9C_3C_2O_1)$, and the out-of-plane CCH_3 angle $\tau_{op} = \tau(H_{12}C_4C_2O_1) = -\tau(H_{15}C_5C_2O_1)$. The three lowest-frequency modes involve rotation of the tery-butyl group, the methoxy group, and the in-plane CCH_3 group, and at the minimum of the potential the three motions are strongly coupled as all three involve significant contribution of the methoxy methyl group. Mode 4 is the symmetric rotation of the out-of-plane CCH_3 groups, and mode 5 is the geared rotation of the three CH_3 groups. Modes 1, 3, and 5 are highly anharmonic; the B3LYP and MP2 VPT2 treatments give positive and/or anomalously large freqency shifts for these modes, even after deperturbation. In particular, vibration-rotation corrections involving mode 1 have a large effect on the relative magnitudes of ΔB and ΔC, and they are extremely sensitive to the level of theory used (see ESI). Moreover, the low harmonic frequency of mode 1 affects the calculation of the quartic and sextic centrifugal distortion constants, as discussed in further detail below. Nevertheless, the calculated harmonic frequencies are in reasonable agreement with the gas-phase experimental values for all modes except mode 1.

3.2 Internal Rotation

The relaxed MP2/ANO0 1D PES scans for the OCH_3, $C(CH_3)_3$, and CCH_3 internal rotations are shown in the ESI, Figure S3. Energies and Cartesian coordinates for each optimized structure along the scan are provided in the ESI, as well as the corresponding results from the MP2/cc-pVDZ calculations. Dihedral angles were shifted by 180° to place the potential minimum at an angle of 0° and the full potential was constructed by exploiting the C_s symmetry of the molecule. The OCH_3 rotation has the lowest barrier (626.3 cm^{-1} from the difference of ab initio energies), while the barriers for $C(CH_3)_3$ (1125.3 cm^{-1}) and CCH_3 (1329.2 cm^{-1}) are considerably higher. Each potential was fitted to the periodic function

$$V(\alpha) = \frac{V_3}{2}\left(1-\cos 3\alpha\right) + \frac{V_6}{2}\left(1-\cos 6\alpha\right). \qquad (1)$$

Results of the fits are also given in the ESI, Figure S3. Inclusion of the V_6 term is necessary to achieve a suitable fit. For the OCH_3 and $C(CH_3)_3$ potentials, the minima near ±120° are noticeably shifted from local C_{3v} symmetry, with deviations of ±40 cm^{-1} with respect to the model. The results are consistent with the experimental observation that splittings arise only from the OCH_3 rotation in the previously measured rotational spectrum of MTBE.[26] On the other hand, the calculated V_3 value for the OCH_3 rotation (631.5 cm^{-1}) is significantly larger than the experimental value of 498.6±3.0 cm^{-1}. As an additional check, a geometry optimization was performed at CCSD(T)/cc-pVTZ with the OCH_3 dihedral angle constrained at 180° away from the minimum, yielding an energy difference of 585.4 cm^{-1}.

As suggested by the normal coordinates at the PES minimum, the OCH_3 and $C(CH_3)_3$ motions are significantly coupled, as shown by the 2D PES in Figure 3. The potential energy surface was fit to Equation 2, which consists of all internal rotation pa-

Param.	MP2/cc-pVDZ	MP2/ANO0	B3LYP/6-311+G(2d,p)	CCSD(T)/cc-pVTZ
A_e	4373.11	4391.64	4374.09	4443.68
B_e	2743.30	2739.14	2712.94	2771.90
C_e	2735.80	2730.64	2709.94	2766.70
ΔA	−50.36	−53.47	−52.92	–
ΔB	−29.79	−30.72	−31.15	–
ΔC	−19.39	−25.10	−29.17	–
A_0	4322.74	4338.17	4321.18	4390.76
B_0	2716.41[a]	2708.42	2681.79	2740.75
C_0	2713.51[a]	2705.53	2680.83	2737.53
$\mu_{a,e}$	0.019	0.071	0.141	0.035
$\mu_{b,e}$	1.163	1.279	1.300	1.207
$\mu_{a,0}$	0.001	–	0.150	–
$\mu_{c,0}$	1.123	–	1.247	–

[a]Upon inclusion of zero-point corrections, the b and c inertial axes in the ground state are reversed with respect to the equilibrium geometry. At equilibrium, the COC angle lies in the ab plane, and in the ground state it lies in the ac plane.
[b]Using ΔB values from B3LYP/6-311+G(2d,p) calculations.

Table 2 Calculated rotational constants and dipole moment projections of MTBE. Rotational constants in MHz and dipole projections in D.

Mode	Sym.	Exp.[42]	Calc.	Int.	Description
1	A''	101	18	2.40	$0.71\tau_t + 0.66\tau_m + 0.18\tau_{ip} - 0.10\tau_{op}$
2	A''	179	178	1.10	$-0.15\tau_t + 0.63\tau_m - 0.34\tau_{ip} - 0.48\tau_{op}$
3	A''	219	238	1.38	$-0.22\tau_t + 0.57\tau_m + 0.76\tau_{ip} + 0.14\tau_{op}$
4	A'	262	262	0.38	$0.68\tau_{op}$
5	A''	274	293	1.73	$-0.23\tau_t + 0.44\tau_m - 0.54\tau_{ip} + 0.47\tau_{op}$

Table 3 MP2/cc-pVDZ torsional vibrational modes and harmonic frequencies of MTBE. Frequencies in cm^{-1} and intensities in km/mol.

Parameter	Value (cm^{-1})
$V_{3,\alpha}$ (OCH_3)	836.06(7)
$V_{6,\alpha}$ (OCH_3)	−71.00(7)
$V_{3,\beta}$ ($C(CH_3)_3$)	1215.73(7)
$V_{6,\beta}$ ($C(CH_3)_3$)	−69.7(7)
V_{cc}	74.88(5)
V_{ss}	−125.84(6)

Table 4 2D potential energy terms for $OCH_3/C(CH_3)_3$ coupled internal rotation. Values in parenthesis are 1σ statistical uncertainties from the fit.

rameters supported by the XIAM$_{mod}$ program.[30]

$$\begin{aligned} V(\alpha,\beta) &= \frac{V_3}{2}\left(1-\cos 3\alpha\right) + \frac{V_6}{2}\left(1-\cos 6\alpha\right) \\ &+ \frac{V_3}{2}\left(1-\cos 3\beta\right) + \frac{V_6}{2}\left(1-\cos 6\beta\right) \\ &+ V_{cc}\cos 3\alpha\cos 3\beta + V_{ss}\sin 3\alpha\sin 3\beta \end{aligned} \quad (2)$$

The results are shown in Table 4. However, this fit has errors as large as ±150 cm^{-1} (ESI Figure S7), especially in the vicinity of the local minima in the outer four quadrants in Figure 3; hence the model likely requires additional higher-order terms in order to better reproduce the ab initio energies. The parameters in the table should therefore be viewed with skepticism.

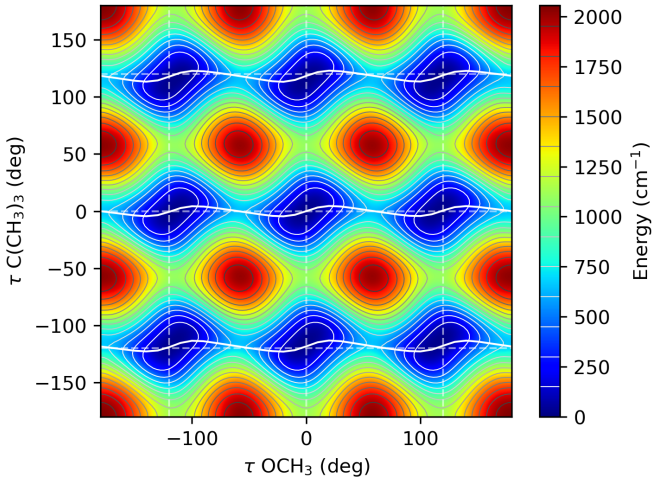

Fig. 3 The 2D MP2/cc-pVDZ PES of MTBE for the coupled rotation of the OCH_3 and $C(CH_3)_3$ groups. Contours are drawn at 150 cm^{-1} intervals, and the dashed gray lines show angles of 0 and ±120°. The minimum energy path for OCH_3 rotation in each $C(CH_3)_3$ well is shown with a solid white line.

3.3 Rotational Spectroscopy

3.3.1 Ground State

The K_a band rotational spectrum of MTBE (Ar, 3.75 bar backing pressure) is shown in Figure 4. The spectrum is dominated by a series of b-type R-branch transitions arising from levels with J'' = 3–7 which show A/E splitting from the OCH_3 internal rotation. When K_a is $\lesssim$2, the b-type A/E doublets are accompanied by a nominally forbidden c-type transition with E symmetry, forming a triplet-like pattern in which the c-type transition appears to "borrow" intensity from the E component of the doublet. Because of the extreme near-prolate nature of the molecule, the asymmetry splitting between the K_c states for a given K_a effectively vanishes by K_a=3 and the molecule behaves like a pure symmetric top with quantum numbers J_k, albeit with a dipole moment perpendicular to the molecular symmetry axis giving a $\Delta|k| = +1$ selection rule. In the A states, the $(J+1)_{-k-1} - J_{-k}$ and $(J+1)_{k+1} - J_k$ transitions are degenerate, but the degeneracy is lifted for E states by terms that couple the methyl rotor angular momentum with the projection of the rotational angular momentum onto the molecular z axis (e.g., $\hat{J}_\alpha \hat{J}_z$). The R-branch transitions form triplets with a 1:2:1 intensity pattern corresponding to the E:2A:E transitions, and the XIAM$_{mod}$ program labels the E components as c-type in the asymmetric top limit.

Three clusters of weak R-branch a-type transitions were also observed from levels with J'' = 4, 5, and 6, as shown in the ESI, Figure S8. The clusters consist of a pair of $K_a = 1$ satellites which display small A/E splitting together with a group of heavily overlapped transitions arising from levels with $K_a \neq 1$. Because of the spectral overlap and interference from different phases in the molecular FID causing an attenuation of the signal, only the $K_a = 1$ satellites were included in the spectroscopic fit. All of these low-J lines (a-, b-, and c-type) were readily predicted and assigned using the constants derived from the previous low-frequency work.[26]

Four Q branches consisting of b- and c-type transitions are present throughout the spectrum near 28, 31, 34, and 37 GHz; these correspond to progressions sharing K_a'' values of 8–11, respectively, and at these values the signed quantum number K is good. An example of the $K'' = \pm 10$ branch in the 3.75 bar Ar spectrum is shown in Figure 5, with J values ranging from 10–31 visible in the figure. Two series of peaks are apparent with a ca. 3:1 intensity ratio. Peaks within the taller series consist of the degenerate A transitions corresponding to $J_{11} - J_{10}$ and $J_{-11} - J_{-10}$ as well as the E component of the $J_{-11} - J_{-10}$ transition which is calculated to lie only a few kHz below its A component, much less than the experimental resolution of $\sim$100 kHz (determined from Gaussian fits of the linewidths of strong, isolated lines in the spectrum). As J increases, the spacing between successive peaks in the series increases from its initial value of ca. 2.5 MHz to nearly 5 MHz over the range shown. Meanwhile, the E component of the $J_{11} - J_{10}$ transition forms a second series displaced by a nearly constant value of 5.3 MHz. The A/E splitting in this latter series effectively creates a second copy of the former offset by a constant amount, resulting in the aliasing pattern observed in the spectrum.

From spectral simulations based initially on the low-frequency constants, it was readily apparent that the spectrum could not be well-modeled by a single temperature. The Q branches follow a temperature of approximately 20 K; however, at that temperature the low-J R branch transitions are far weaker than the experimental spectrum. Simulations shown in Figures 4–5 are based on an equal admixture of a 7 K component with a 20 K component and employ the dipole moments determined from Stark shift measurements (μ_a = 0.107 D, μ_b = 1.242 D).[26]

Fitting proceeded initially using the 3.75 bar Ar spectrum, and was then supplemented with higher-J transitions from the 1.0 bar Ar spectrum (discussed further below). Each transition was fit to a Gaussian lineshape function, including blended transitions. Uncertainties were estimated based on the signal-to-noise ratio and the presence of blends: for strong, isolated lines the minimum uncertainty was set to 10 kHz, but larger uncertainties up to 70 kHz were used for weak and/or strongly overlapping transitions. Ultimately a total of 1273 transitions were assigned to 704 unique frequencies, including the 32 frequencies reported in Ref. 26. Spectroscopic constants, including quartic and partial sextic centrifugal distortion constants and internal rotation parameters F_0, V_3, and δ were derived by least squares fitting to both Watson's asymmetric (A) and symmetric (S) reduced effective Hamiltonian,[43] both yielding least squares weighted standard deviations below 9 kHz and a root-mean-square deviation of 17.0 kHz. Table 5 shows the spectroscopic parameters for both fits to the ground vibrational state compared with those of Ref. 26 and the quantum chemical calculations. The A reduction in the I^r representation is known to break down as $B - C$ becomes small compared with the R_6 distortion constant.[44–46] The A reduction parameters are shown in Table 5 for the purpose of comparison with the previous work and they agree quite well (within uncertainty). However it is clear that the A reduction is breaking down given the near-prolate nature of MTBE, as δ_K is calculated to be an order of magnitude larger than the other quartic distortion constants yet was not determinable in the fit. The S reduction is more appropriate for a nearly-symmetric molecule, and therefore only the S reduction results will be discussed going forward. After testing different combinations of sextic distortion constants, it was determined that only H_{JK} and H_{KJ} made a meaningful improvement in the fit. The remaining sextic constants were held at the B3LYP/6-311+G(2d,p) values.

The agreement between the experimental and computed quartic centrifugal distortion constants at the B3LYP/6-311+G(2d,p) level is adequate, but the deviations of 20–30% for D_{JK} and D_K are somewhat larger than expected given the large data set and range of quantum numbers spanned by the experimental spectrum. These deviations are caused by the flatness of the potential energy surface along the lowest-frequency normal coordinate. Table S2 in the ESI shows a comparison of the centrifugal distortion constants evaluated at the three levels of theory employed here along with the lowest harmonic frequency ω_{tBu} as a proxy for the potential shape. At MP2/cc-pVDZ, ω_{tBu} is only 18 cm^{-1} and D_{JK} and D_K are each calculated to be an order of magnitude larger than the experimental values. These quartic constants become smaller by about a factor of 3 at MP2/ANO0 (ω_{tBu} = 32 cm^{-1})

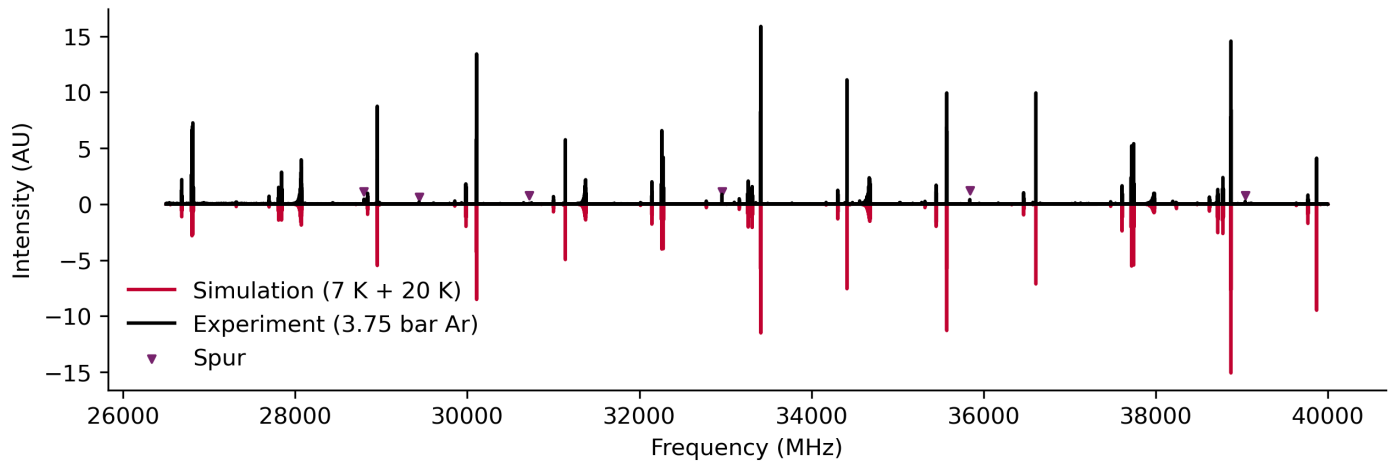

Fig. 4 K_a band spectrum of MTBE with a backing pressure of 3.75 bar Ar (black). The simulated spectrum is based on the S-reduction fit in Table 6, and consists of roughly equal amounts of a 7 K component and a 20 K component. Spurious signals arising from the spectrometer digital signals are marked with purple triangles.

Parameter	Previous[26]	A reduction	Calc. (A)[a]	S reduction	Calc. (S)[a]
A_0 (MHz)	4382.840(2)	4382.83984(12)	4390.76	4382.84023(12)	4390.76
B_0 (MHz)	2732.3925(7)	2732.39255(10)	2740.75	2732.39279(11)	2740.75
C_0 (MHz)	2730.7545(8)	2730.75659(10)	2737.53	2730.75633(11)	2737.53
Δ_J/D_J (kHz)	0.301(22)	0.32351(52)	0.345	0.32352(51)	0.329
Δ_{JK}/D_{JK} (kHz)	4.08(21)	4.21373(16)	4.99	4.212900(13)	5.09
Δ_K/D_K (kHz)	−3.29(27)	−3.66480(56)	−4.45	−3.65752(55)	−4.53
δ_J/d_1 (kHz)	0.023(18)	0.00587(37)	0.00684	−0.00512(37)	−0.00684
δ_K/d_2 (kHz)	[0.0]	[0.0]	35.7	−0.0118(12)	−0.00800
Φ_J/H_J (Hz)	[0.0]	[0.00005]	0.00005	[0.000048]	0.000048
Φ_{JK}/H_{JK} (Hz)	[0.0]	0.01119(7)	−0.218	0.01096(4)	0.0269
Φ_{KJ}/H_{KJ} (Hz)	[0.0]	−0.0147(8)	0.752	−0.0174(7)	−0.0571
Φ_K/H_K (Hz)	[0.0]	[0.0]	−0.536	[0.0304]	0.0304
ϕ_J/h_1 (Hz)	[0.0]	[0.000002]	0.000002	[0.000016]	0.000016
ϕ_{JK}/h_2 (Hz)	[0.0]	−0.120(12)	−0.215	[0.0000005]	0.0000005
ϕ_K/h_3 (Hz)	[0.0]	[0.0]	−103.0	[−0.000014]	−0.000014
V_3 (cm^{-1})	498.6(30)	494.94(25)	631.5(42)	494.77(25)	631.5(42)
F_0 (cm^{-1})	5.268(33)	5.2308(25)	5.233	5.2292(24)	5.233
δ (°)	26.07(40)	26.373(29)	26.27	26.399(29)	26.27
σ (kHz)[b]	–	8.8		8.6	
RMS (kHz)[c]	1.3	17.1		17.0	
$\mathrm{RMS}^d_{\mathrm{red}}$	0.65	0.64		0.63	
N^e_{f}	32	704		704	
$J''_{\mathrm{max}}/J''_{\mathrm{min}}$	3/1	64/1		64/1	
$K''_{a,\mathrm{max}}/K''_{a,\mathrm{min}}$	2/0	11/0		11/0	

[a]Rotational constants are CCSD(T)/cc-pVTZ B_e corrected by B3LYP/6-311+G(2d,p) ΔB values. F_0 and δ are from the CCSD(T)/cc-pVTZ equilibrium structure, and V_3 is the MP2/ANO0 value. Centrifugal distortion constants are from B3LYP/6-311+G(2d,p) calculations.
[b]Weighted standard deviation of least squares fit.
[c]Root mean square deviation of observed and calculated frequencies.
[d]Reduced mean square deviation of observed and calculated frequencies weighted by uncertainty.
[e]Number of unique frequencies in the fit.

Table 5 Spectroscopic parameters of MTBE in the ground vibrational state (I^r representation). Quantities in square brackets were fixed in the fit.

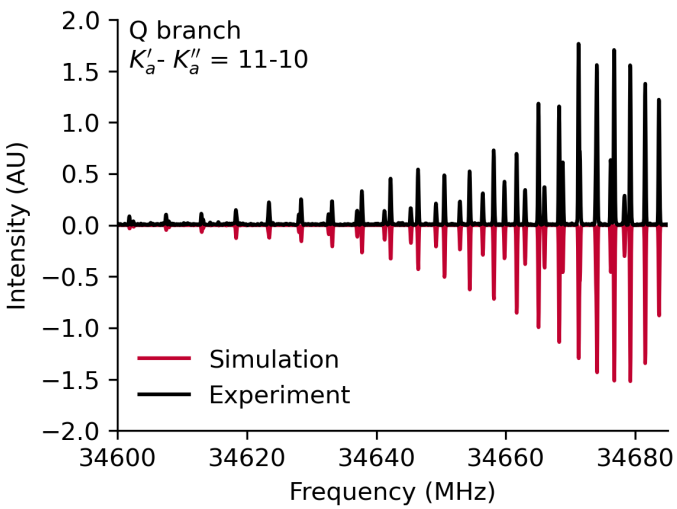

Fig. 5 MTBE spectrum (3.75 bar Ar) showing Q branch transitions of MTBE with $K_a'' = 10$ originating near 34680 MHz.

and then a factor of 3 smaller still at B3LYP/6-311+G(2d,p) (ω_{tBu} = 58 cm^{-1}). Even the B3LYP calculations overestimate the magnitudes of D_{JK} and D_K, however, suggesting the computed values remain in error due to the flat potential. The situation is even more dramatic for the sextic constants, nearly all of which undergo order-of-magnitude-level changes at each level of theory. This likely accounts for the factor of 3–4 difference in the determined values of H_{JK} and H_{KJ} between experiment and theory.

3.3.2 Torsionally Excited State

Just toward lower frequency of each of the Q branches in the 3.75 bar Ar spectrum, a second very weak Q branch was observed which we assumed corresponded to a torsionally excited state of the OCH_3 rotor. To further investigate, and to extend the range of J values observable in the Q branches of the ground vibrational state, we decreased the backing pressure of the Ar gas as low as possible to a nominal value of 1 bar, which was just above the vapor pressure of MTBE (0.33 bar at 25 °C). Nevertheless, the colder 7 K component remained, albeit at a reduced level. The simulated spectrum shown in Figure 6 is composed of 7 K and 45 K components in a ca. 1:3 ratio.

Identification and assignment of the torsionally excited state was facilitated by identification of R-branch triplets with large K_a and an increased A/E splitting. An example is shown in Figure 7, where the $J_{|k|} = 5_4 - 4_3$ triplets for the ground and torsionally excited states can be seen near 38870 MHz. However, assignment of R-branch transitions with $K_a'' = 0$ proved to be more challenging. In the ground state, an A/E doublet corresponding to the $7_{17} - 6_{06}$ transition can be seen at 39689 MHz, which lies just to higher frequency than the $5_4 - 4_3$ triplet. Another A/E doublet with an increased splitting was seen nearby at 39957 MHz and was initially assigned to $7_{17} - 6_{06}$, but a satisfactory fit could not be obtained together with the higher K_a transitions. We soon noticed that the predicted spectrum from our preliminary fit did contain another A/E doublet extremely close to 39957 MHz: the $7_{16} - 6_{06}$ c-type transition. By making this assignment and switching the dipole projection from μ_b to μ_c, the low-K_a'' transitions throughout the spectrum could be immediately identified with the correct intensities. To best facilitate a simultaneous fit, the larger dipole moment component was set to the molecular x axis, and the I^r representation was used for the ground vibrational state while the I$^\ell$ representation was used for the upper state. This "axis-switching" effect will be discussed in more detail in the following section.

With the low-J transitions assigned, the Q branches were able to be assigned. The $K_a'' = 8$ Q branch of the $v_t = 1$ state near 28 GHz, which is embedded within the corresponding ground-state Q branch, is shown in Figure 8. Its origin is the pair of overlapped $9_{\pm 9} - 8_{\pm 8}$ A symmetry transitions at 28007.4 MHz. The $9_{-9} - 8_{-8}$ E component is shifted down by 2.7 MHz, while the $9_9 - 8_8$ E component is shifted up by 22.4 MHz, forming the origin of a higher-frequency comb of transitions. Additional transitions presumably corresponding to the $v_t = 2$ state are visible in the spectrum; however, owing to their low intensity and the heavy spectral congestion, no effort has been made to assign them.

A total of 701 transitions and 407 unique frequencies were added to the ground-state transitions and simultaneously fit using the S reduction to an overall RMS deviation of 10.7 kHz and a maximum deviation of 2.98σ (Table 6). For the two-state fit, the V_6 term was added to the Hamiltonian and the H_J, V_3, V_6 and F_0 parameters were constrained to be equal in both states. Compared with the single-state fit, the ground-state parameters in the two-state fit all agree within uncertainty with the exception of V_3, as discussed in more detail below. Because of the change in representation between the two states, the b and c inertial axes are swapped between the two fits. The $B_v - B_0$ shifts are therefore $\Delta B_z = -1.49101(35)$, $\Delta B_x = -0.34682(42)$, and $\Delta B_y = 4.14671(52)$ MHz.

3.3.3 Isotopologues and r_0 Structure Determination

Returning to the colder spectrum, the signal-to-noise ratio on the R-branch transitions was sufficient for observing the singly-substituted ^{13}C isotopologues in natural abundance. In order to observe the ^{18}O isotopologue, an additional spectrum was recorded using Ne carrier gas and a heated source as previously described to increase signal, and the spectrum was integrated for a longer duration. Ultimately, all heavy atom isotopologues were identified in this spectrum in natural abundance, as shown in the ESI, Figure S9. Lines from each isotopologue were combined with those reported in Ref. 26 and fit to the Watson S-reduced effective Hamiltonian; results are shown in Table 7. In the analysis, only the rotational constants and rotor angle(s) were fit; the remaining parameters were all set to their corresponding values in the single-state fit shown in Table 6. Among these, the ^{18}O isotopologue shows the poorest fit; the transitions with the greatest weighted deviation are the $3_{03} - 2_{12}$ A/E doublet measured in Ref. 26, where the splitting is underestimated by ca. 23 kHz. This fit also has a systematic positive deviation of 14 kHz, which could likely be addressed by adjusting centrifugal distortion terms; however, owing to the low signal-to-noise ratio in the K$_a$ band data and the small number of lines in the fit, these terms were nevertheless held constant.

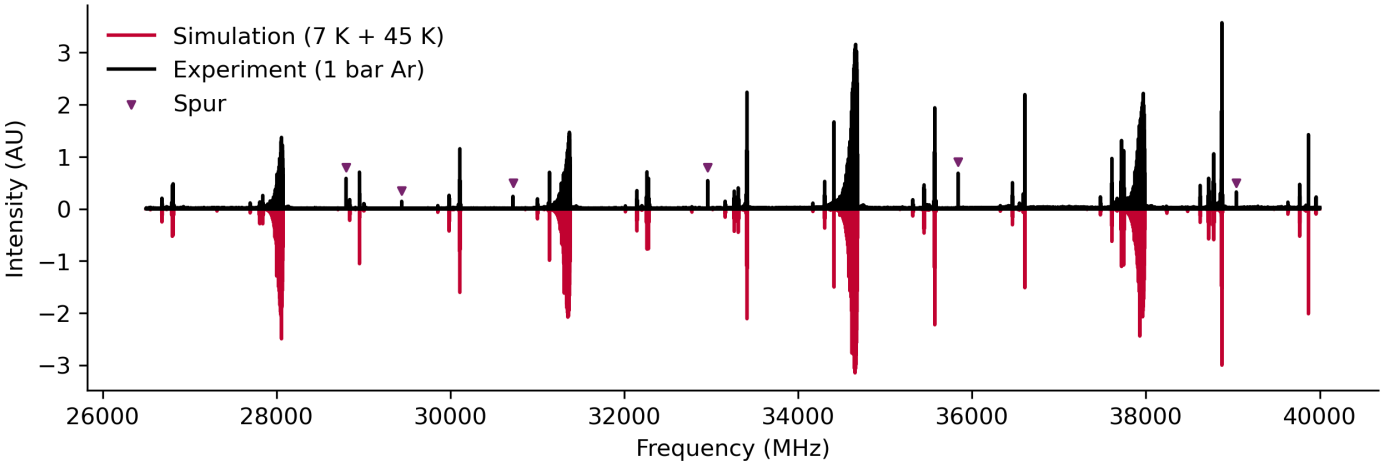

Fig. 6 K_a band spectrum of MTBE with a backing pressure of 1 bar Ar (black). The simulated spectrum is based on the S-reduction fit in Table 6, and consists of 7 K and 45 K components in a roughly 1:3 ratio. Spurious signals arising from the spectrometer digital signals are marked with purple triangles.

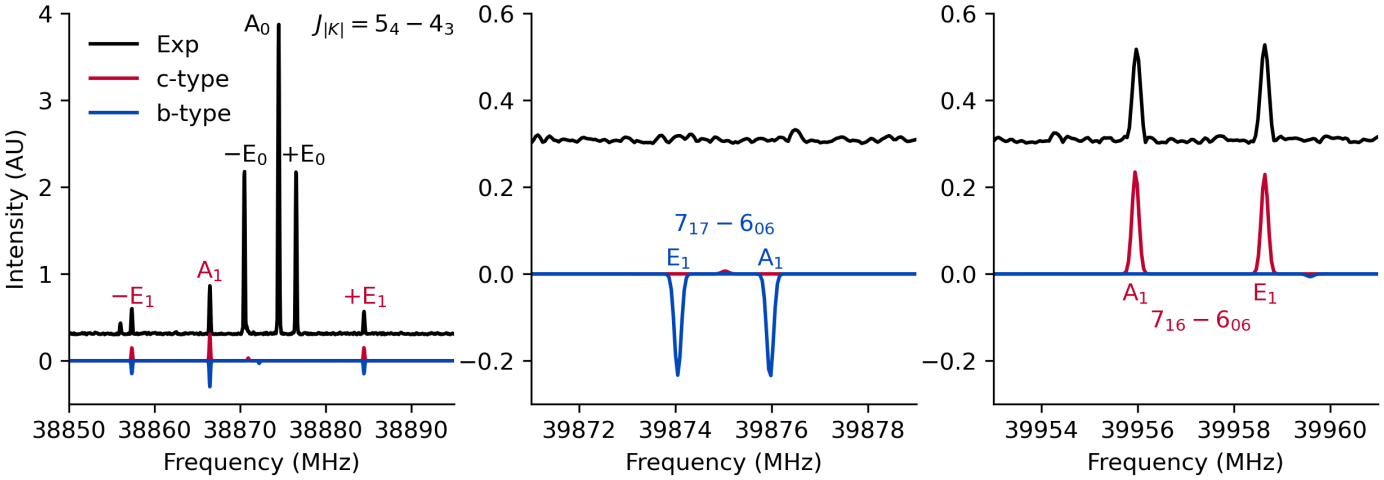

Fig. 7 (left) $J_k = 5_{\pm 4} - 4_{\pm 3}$ transition of MTBE in the ground and torsionally excited states. The $+$ and $-$ labels on E correspond to the sign of K, and subscripts indicate the v_t quantum number. (center) Experimental spectrum at the location of the b-type $7_{17} - 6_{06}$ transition in the torsionally excited state. (right) Experimental spectrum at the location of the c-type $7_{16} - 6_{06}$ transition in the torsionally excited state. In all three panels, the red trace corresponds to a simulation with the dipole moment aligned to the c axis, while the downward blue trace shows a simulation with the dipole moment aligned to the b axis. The experimental spectrum has been offset by 0.3 units for clarity.

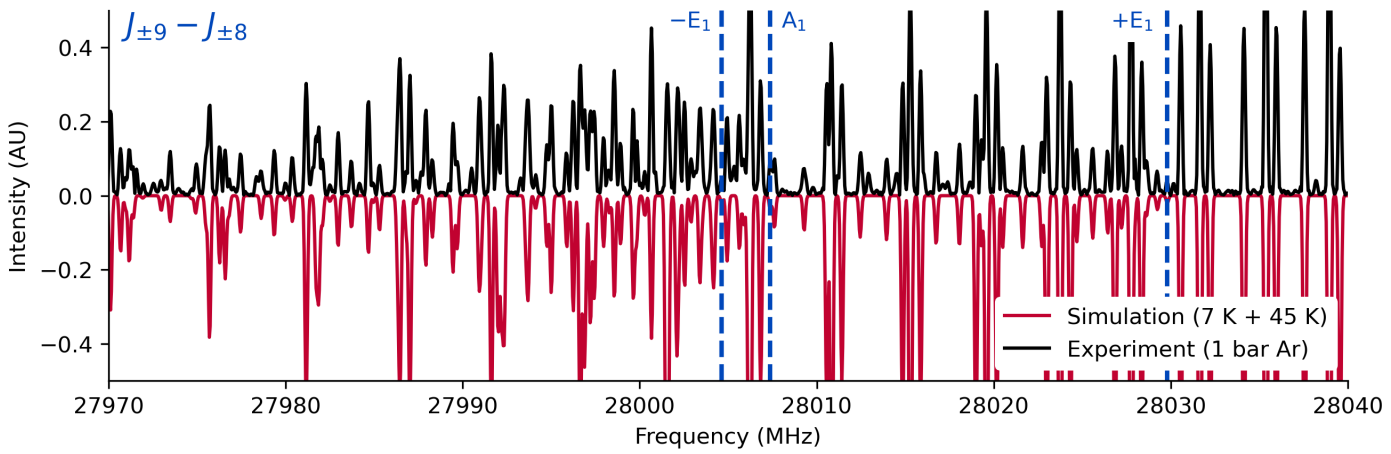

Fig. 8 As Figure 6, zoomed on the $K_a'' = 8$ b-type Q-branch of the torsionally excited state near 28 GHz. The origins of the $J_{\pm9} - J_{\pm8}$ A and E components are indicated with blue dashed lines. Additional unassigned lines, likely arising from the $v_t = 2$ state, are visible in the experimental spectrum.

		Combined fit	
Parameter	Single-state fit	$v = 0$, I^r	$v = 1$, I$^\ell$
A (MHz)	4382.84023(12)	4382.84023(13)	4381.34922(32)
B (MHz)	2732.39279(11)	2732.39284(12)	2734.90299(40)
C (MHz)	2730.75633(11)	2730.75628(12)	2732.04602(51)
D_J (kHz)	0.32352(51)	0.32352(57)	0.3206(29)
D_{JK} (kHz)	4.212900(13)	4.21289(15)	1.58137(49)
D_K (kHz)	−3.65752(55)	−3.65742(62)	−1.0110(16)
d_1 (kHz)	−0.00512(37)	−0.00511(42)	0.0231(22)
d_2 (kHz)	−0.0118(12)	−0.0118(14)	−0.1380(22)
H_J (Hz)	[0.000048]	[0.000048]	[0.000048]
H_{JK} (Hz)	0.01096(4)	0.01096(5)	−0.00634(26)
H_{KJ} (Hz)	−0.0174(7)	−0.0174(8)	0.0223(28)
H_K (Hz)	[0.0304]	[0.0304]	[0.0304]
h_1 (Hz)	[0.000016]	[0.000016]	[−0.000016]
h_2 (Hz)	[0.0000005]	[0.0000005]	[0.0000005]
h_3 (Hz)	[−0.000014]	[−0.000014]	[0.000014]
V_3 (cm^{-1})	494.77(25)	795.72(22)^a	795.725(22)^a
V_6 (cm^{-1})	[0.0]	−382.63(13)^a	−382.63(13)^a
F_0 (cm^{-1})	5.2292(24)	5.2289(13)^a	5.2289(13)^a
δ (°)	26.399(29)	26.395(23)	26.459(18)
σ (kHz)^b	8.3	–	–
RMS (kHz)^c	16.9	17.0	28.6
RMS$^d_{\text{red}}$	0.602	0.62	0.84
N_f^e	704	704	407
$J''_{\text{max}}/J''_{\text{min}}$	64/1	64/1	49/3
$K''_{a,\text{max}}/K''_{a,\text{min}}$	11/0	11/0	11/0
Combined σ (kHz)		10.7	
Combined RMS (kHz)		21.8	
Combined RMS$_{\text{red}}$ (kHz)		0.694	

[a] Fit simultaneously in both states.
[b] Weighted standard deviation of least squares fit.
[c] Root mean square deviation of observed and calculated frequencies.
[d] Reduced mean square deviation of observed and calculated frequencies weighted by uncertainty.
[e] Number of unique frequencies in the fit.

Table 6 S-reduced spectroscopic constants of MTBE in the ground and torsionally excited state.

Among the heavy atom isotopologues, only one substitution involves an atom outside the symmetry plane: ^{13}C4 (or, equivalently, ^{13}C5). Because two equivalent substitutions are possible, the initial spectral simulation generated after fitting was multiplied by twice the natural abundance of ^{13}C (i.e., 2×0.01); however the intensity agreement was poor in several regions of the spectrum. In addition, several additional splittings were observed for low-K_a c-type transitions, and these c-type transitions were stronger than b-type transitions sharing the same lower energy level. An example involving the $J_K = 5_2 - 4_1$ family of transitions is shown in Figure 9. At this low K_a value, in the MTBE parent species a nominally forbidden c-type transition of E symmetry accompanies each b-type A/E doublet and appears to borrow intensity from the E component of the b-type doublet. However, in the analogous transitions for the ^{13}C4 isotopologue, each c-type transition also appears as a clear A/E doublet with equal intensity, and is stronger than the b-type doublet from the same lower level.

These differences in the spectra arise from the extreme near-prolate nature of MTBE: off-axis substitutions cause a large rotation of the inertial axes relative to the parent species. The rotation is illustrated in Figure S10, which shows the structure of ^{13}C4-MTBE viewed in the bc plane (based on the CCSD(T)/cc-pVTZ equilibrium geometry). Compared with the parent species, the OCH_3 group is rotated by ca. 45° from the b axis, and because the major component of the dipole moment points in the direction of the O atom, the dipole moment is also rotated. In addition, the rotation axis of the OCH_3 methyl rotor is no longer in the ab plane, necessitating the introduction of an ε parameter into the fit to account for the angle made by the projection of the rotor axis in the bc plane with respect to the b axis. This parameter was not included in the previous work, leading to comparatively large errors in their least squares fit.[26] From the equilibrium molecular structure, it is clear that ε also gives the rotation of the μ_b dipole component into the bc plane. Because this angle is close to 45°, the μ_b component in ^{13}C4 is roughly a factor of $\sqrt{2}$ smaller than that of the parent, reducing the intensities of those transitions

Parameter	^{13}C0	^{13}C2	^{13}C3	^{13}C4	^{18}O
A (MHz)	4382.84405(26)	4383.28832(30)	4344.63353(31)	4295.23973(28)	4341.74830(95)
B (MHz)	2674.14480(21)	2730.10188(19)	2698.69661(24)	2727.45581(22)	2714.07441(74)
C (MHz)	2672.58403(17)	2728.45866(22)	2682.56521(22)	2693.67817(19)	2696.75160(59)
δ (°)	27.281(29)	26.344(35)	25.093(23)	26.920(22)	30.422(68)
ε (°)	[0.0]	[0.0]	[0.0]	51.2(13)	[0.0]
σ (kHz)[a]	4.5	5.3	5.3	6.6	8.5
RMS (kHz)[b]	17.8	20.8	23.4	26.0	35.7
RMS$_{red}$[c]	0.49	0.59	0.63	0.64	1.17
N_f[d]	54	49	59	85	24

[a]Weighted standard deviation of least squares fit.
[b]Root mean square deviation of observed and calculated frequencies.
[c]Reduced mean square deviation of observed and calculated frequencies weighted by uncertainty.
[d]Number of unique frequencies in the fit.

Table 7 Spectroscopic parameters for MTBE heavy-atom isotopologues (S reduction). Centrifugal distortion constants and the internal rotation barrier were held fixed at the ground-state values shown in Table 5. Quantities in square brackets were fixed in the fit.

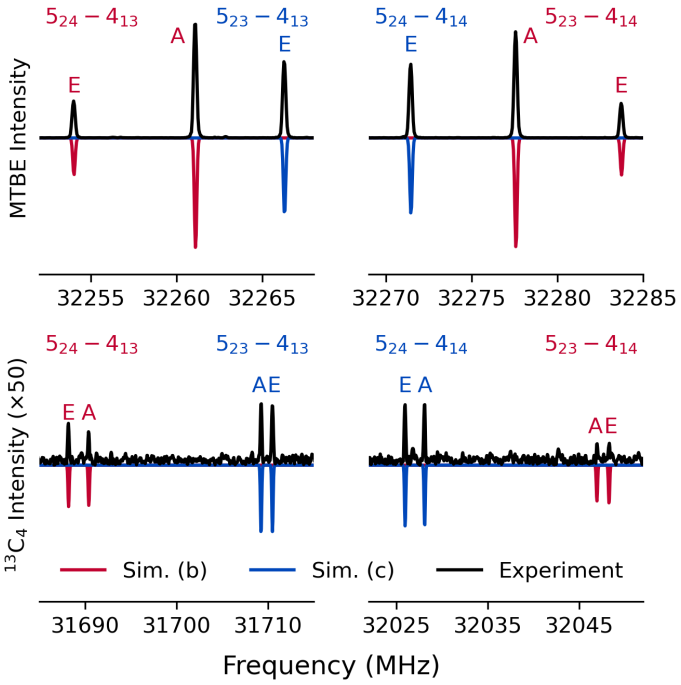

Fig. 9 Comparison of $J_K = 5_2 - 4_1$ transitions for MTBE (top panels) and the ^{13}C4 isotopologue scaled by a factor of 50 (bottom panels) and spectral simulations indicating b- and c-type transitions (red and blue, respectively). The dipole projections for the ^{13}C4 isotopologue in the simulation ($\mu_b = 0.777$ D and $\mu_c = 0.969$ D) correspond to a rotation of the MTBE μ_b component (1.242 D) by the fitted value of ε (51.3°) about the a axis, and the simulation intensity is multiplied by 2×0.01 to account for the natural abundance of ^{13}C and the two equivalent substitutions at C$_4$ and C$_5$.

by a factor of 2 and offsetting the factor of 2 increase from the equivalent positions. At the same time, c-type transitions become allowed, resulting in new peaks from states with low-K_a. Nevertheless, as K_a'' becomes $\gtrsim$3, the asymmetry splitting approaches 0 and the triplet E:2A:E structure is recovered, yielding peaks that are a factor of 2 stronger than analogous peaks from other ^{13}C isotopologues. This effect can be seen in Figure S9 in the 32–33.5 GHz region. Near 32 GHz are the $5_2 - 4_1$ R-branch transitions, where all ^{13}C isotopologues have equal intensity but the ^{13}C4 isotopologue shows 2 peaks. In the 33–33.5 GHz region, the $4_4 - 3_3$ transitions for ^{13}C4 are twice as strong as the corresponding transitions from the other ^{13}C species as the b- and c-type transitions overlap at the experimental resolution. The combination of the ε parameter from the least squares fit with the relative intensities of b/c-type pairs of transitions sharing a lower state (Figure 9) provide an internal consistency check on the agreement between the molecular structure and the spectrum.

Using the experimental rotational constants of MTBE and the isotopologues measured here, the heavy-atom r_0 structural parameters were determined by least squares fitting to ground-state moments of inertia using the STRFIT program.[31] The results are shown in Table 8; for this structure, all internal coordinates involving the position of a hydrogen atom were held at the computed CCSD(T)/cc-pVTZ values. Additionally, the C_s symmetry was enforced by constraining the parameters involving C5 to be equal to the analogous quantities involving C4 except the dihedral angle, which was constrained to have the opposite sign. Unlike in Ref. 26 no difficulties were encountered with linear dependence among the structural parameters and a complete r_0 structure involving the heavy atoms was determined.

4 Discussion

Figure 10 shows the relative power of the spectrometer across the K$_a$ band, along with a spectrogram of the chirp, as obtained by recording a 10 μs duration chirp leaking through the protection switch in the open position. As such, effects of the downconversion electronics also contribute to this response, in addition to the power variation of the chirp itself. The overall response of

Parameter	r_0 Previous[26]	r_0 This Work	r_e MP2/cc-pVDZ	r_e CCSD(T)/cc-pVTZ
$R(C_0O_1)$	[1.415][a]	1.4154(28)	1.4136	1.4090
$R(O_1C_2)$	[1.417][a]	1.4384(79)	1.4385	1.4317
$R(C_2C_3)$	1.498(4)	1.5412(90)	1.5269	1.5183
$R(C_2C_4)$	1.567(2)	1.5295(65)	1.5320	1.5237
$\angle(C_0O_1C_2)$	118.5(5)	116.51(41)	116.12	116.09
$\angle(O_1C_2C_3)$	106.3(3)	102.76(68)	102.98	103.57
$\angle(O_1C_2C_4)$	110.9(3)	111.35(32)	111.33	111.10
$\tau(C_4C_2O_1C_3)$	117.6(3)	117.41(50)	117.91	118.15

[a]Quantities in square brackets were held fixed.

Table 8 Comparison of r_0 and calculated structural parameters of MTBE. Values in parentheses at 1σ statistical uncertainties in units of the last digit.

the instrument increases smoothly by approximately 5 dB from 26.5 to 40 GHz, as shown on the left side of the figure. In the panel on the right, a spectrogram of the chirp's power spectrum as a function of time is shown. The spectrogram was generated from the squared Fourier transform taken in 1000 point bins (i.e., 20 ns intervals) and shows minimal contamination from interactions with other harmonics of local oscillator signals; they are at lesat 15–20 dB weaker than the primary chirp at all times.

The overall gain flatness and spectral purity are reflected in the good agreement of the intensities in Figures 4, 5, and 6 with the simulated spectra. With the exception of the overlapping a-type transitions in Figure S8, the factor of $\sim$2 intensity agreement between the experimental spectrum and the simulation reflects the gain variation observed in the chirp power spectrum. Interestingly, the combs of Q-branch transitions in Figure 5 show intensity variations over short frequency ranges that resemble a type of standing wave pattern. Nevertheless, the overall performance over the entire frequency range is satisfactory for determining rotational temperatures and relative abundances. One potential improvement might arise from applying a frequency-dependent correction factor using the data in the left panel of Figure 10; this has not been pursued at present. In addition, only a small number of spurious frequencies ($<$10) are present throughout the spectrum and they are readily identified by their frequencies and their sharpness. In the absence of the Hanning window function, the spurs occupy only a single frequency bin as long as they are an integer multiple of 10 MHz. They occur at offset frequencies that are based on combinations and multiples of the 6.25 GHz sampling rate of the raw analog-digital converters in the oscilloscope, the 16 GHz sampling rate of the digital-analog converter in the AWG, and the two LO base frequencies of 5120 MHz and 5760 MHz.

Similar to the analysis of the low-J spectrum of MTBE,[26] the ground-state fit determined here yields a V_3 OCH_3 internal rotation barrier of 494.82$\pm$0.24 cm^{-1}, which is considerably lower than the MP2/cc-pVDZ value of 630 cm^{-1}. The calculated internal rotation potential; however, suggests a significant negative V_6 term. When including the torsionally excited state in the fit; however, the V_3 term increases dramatically to nearly 800 cm^{-1}, while the V_6 term is fitted to a value of just below $-$380 cm^{-1}. A V_6 term of this magnitude does not seem physically plausible; this would imply that the equilibrium geometry corresponds to a C_1 geometry with the OCH_3 rotor misaligned with respect to the *tert*-butyl group. Such a situation has been observed for the structurally similar molecule pinacolone ($CH_3C(=O)C(CH_3)_3$),[47] which differs from MTBE by replacing the oxygen atom with a carbonyl group. In addition to having a C_1 equilibrium geometry, the barrier at the C_s geometry for pinacolone is comparable to the internal rotation barrier of the terminal CH_3 group (both ca. 150 cm^{-1}), which results in a quasi-sixfold potential barrier. Careful searches for a lower-lying minimum of C_1 symmetry were carried out at the MP2/cc-pVDZ, MP2/cc-pVTZ, and CCSD(T)/cc-pVTZ levels of theory, using both the native optimizer in CFOUR and the optimizer in GeomeTRIC; all converged to C_s. Also unlike pinacolone, here the fit to both A and E states in both torsional states were well-predicted by the XIAM$_{mod}$ program, and no strong lines observed in the spectrum remain unassigned.

However, the 2D PES shown in Figure 3 shows that the OCH_3 and *tert*-butyl internal rotation motions are coupled in a manner similar to, but less extreme than, pinacolone. Preliminary efforts were made to introduce the *tert*-butyl group as a second rotor into the XIAM$_{mod}$ fit, but these were quickly abandoned as inclusion of the rotor parameters based on the CCSD(T)/cc-pVTZ structure immediately altered the spectral patterns beyond recognition owing to a large calculated F_{12} parameter. In addition, other potential internal rotation motions involving the CH_3 units on the *tert*-butyl group were explored but none possessed either a low barrier or asymmetric well shapes near the equilibrium geometry similar to those in Figure 3. Instead, the fit is treating the system as a quasi-1D rotor involving a pure CH_3 rotation, and this difference likely accounts for the large effective V_6 magnitude observed in the fit. It is also possible that inclusion of a V_9 term may bring down both V_3 and V_6 to values closer to the MP2 predictions; however the XIAM$_{mod}$ program lacks this capability at the present time.

The near-prolate nature of MTBE gives rise to multiple interesting spectroscopic patterns, including the strong forbidden c-type transitions that accompany the low-K_a'' b-type A/E doublets and the collapse of the asymmetry splitting at comparatively low values of K_a'' as previously shown. In the ground state, the asymmetry parameter is $-$0.99802 and in the torsionally excited state, it is $-$0.99654. MTBE is not the closest known molecule to an accidental symmetric top; deuterated disulfane (DSSD)[48] has B_0 and C_0 values which differ by only 0.02 MHz ($\kappa = -0.99999932$).

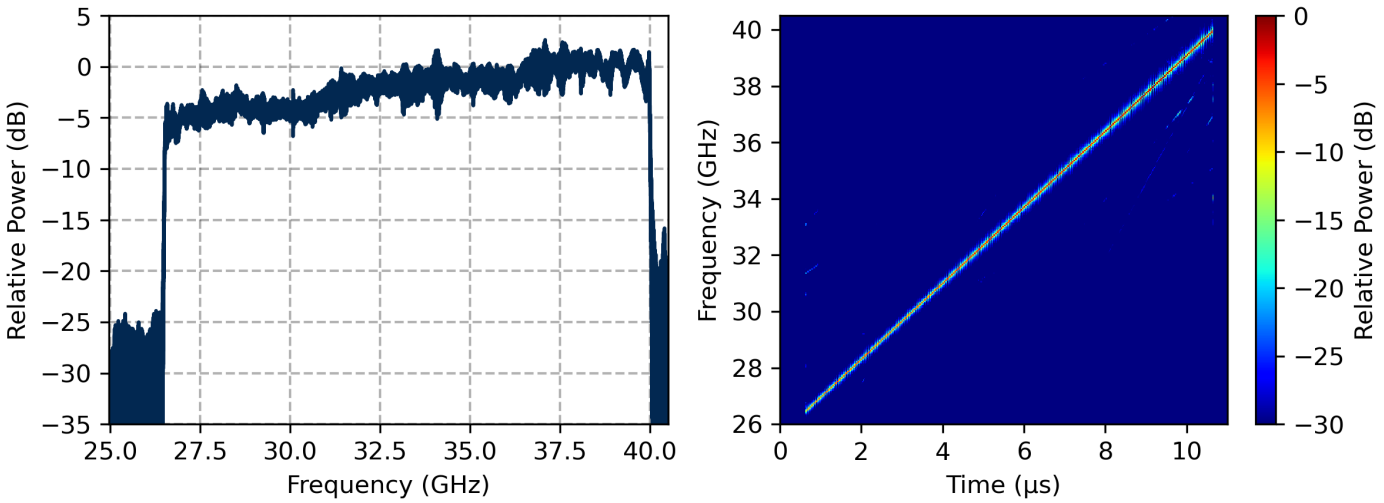

Fig. 10 (left) Relative power spectrum of a 10 μs chirp as a function of frequency. (right) Relative power spectrogram of a 10 μs duration chirp in chunks of 20 ns.

DSSD (along with its other isotopologues) is a classic case of an accidental prolate symmetric top, featuring anomalous K-doubling from centrifugal distortion and was one of the test cases for the breakdown of the A-reduced effective Hamiltonian.[49–52] Nevertheless, it does not possess internal rotation motion and its spectrum is purely c-type. Low-lying torsionally excited states of DSSD corresponding to its scissor-like motion have been observed; these increase the DSSD dihedral angle and move the system away from the prolate limit, but extrapolation suggests that at the equilibrium geometry DSSD is a perfect accidental symmetric top to within experimental uncertainty. Despite its drastically different structure, which may not even initially appear prolate at all at first glance, MTBE has similarities to DSSD especially with regard to the treatment of centrifugal distortion. However unlike DSSD, torsional excitation of MTBE swaps the b and c inertial axes; this implies that the structures of each of the two vibrational states lie on opposite sides of the pure prolate limit. We suspect that this is due to both the coupling between the OCH_3 and *tert*-butyl motions and the slight deviations of both rotors from local C_{3v} symmetry. Upon excitation of the OCH_3 torsional mode, the shift in the more massive *tert*-butyl group is sufficient to cause the reorientation of the inertial axes.

A related effect of "vibrationally-induced rotational axis switching" (VIRAS)[53] has been invoked to account for intensity alterations observed in rovibrational spectra of HDCO,[54] BF_2OH,[55] HNO_3,[56] and N_2H_4.[57] In these systems, vibrational motion along certain coordinates (e.g., the OH torsional motion in HNO_3) causes a rotation of the principal axis framework by tens of degrees relative to the Eckart frame between the two vibrational states involved in the transition, particularly when large-amplitude motion is involved. However in those cases the vibrational motion causes a major reorientation of the rotational quantization axis, which in turn leads to a breakdown of the significance of the K quantum number via a $\{J_z, J_x\}$ interaction. In MTBE, the torsional motions have only a minimal affect on the quantization (a) axis. Instead, the orientation of the O atom, and hence, the dominant contribution to the molecular dipole moment, is affected. Due to the C_s symmetry, the O atom must lie either in the ab or ac plane when averaged over the small-amplitude vibrations, so the rotational spectrum in the low-K_a states of A symmetry must be purely b-type (as in the ground state) or c-type (as in the torsionally excited state) as observed experimentally. This type of axis switching effect occurs as the b and c axes become degenerate and change definition due to a slight mass rearrangement, rather than a rotation of the inertial axis system. The Hamiltonian used in the two-state fit contains no terms which are off-diagonal in the v_t quantum number; if such terms were to be introduced, care would need to be taken in evaluating those off-diagonal matrix elements.

While nearly all spectroscopic features in the "cold" MTBE spectra have been assigned; the warm spectrum displays additional transitions in the vicinity of both the Q and R branches. We suspect that these arise from the $v_t=2$ state; they show somewhat similar structure to the $v_t=1$ state but with substantially larger A/E splittings. However, the signal-to-noise ratio of these features was too weak to allow a proper investigation, especially in the vicinity of the Q branches where many transitions overlap with both the $v_t=0$ and $v_t=1$ states. Further spectroscopy in this area with a higher-resolution cavity FTMW spectrometer may allow for this state to be assigned; this would provide a strong test for the predictive capabilities of the present fit by comparing the ΔB values and the trends in the centrifugal distortion constants with increasing v_t.

Finally, the r_0 substitution structure derived here addresses a discrepancy between the previously-reported microwave structure[26] and the structure derived from electron diffraction measurements.[28,29] The latter measurements, in agreement with the theoretical calculations here, found that the CC distances within the *tert*-butyl group were all nearly equal (~1.530 Å), while the former found that the in-plane CC distance (1.498 Å) was nearly 70 mÅ shorter than the out-of-plane distance (1.567 Å). Our r_0 structure is in excellent agreement with the electron diffrac-

tion measurements for these two distances: 1.541±0.009 Å and 1.530±0.007 Å for the in- and out-of-plane groups, respectively. This may be in part due to the constraints imposed on the two CO distances in the previous microwave work; the length of 1.417 Å assigned to the CO distance on the *tert*-butyl side is about 20 mÅ shorter than the present r_0 value of 1.438 Å. However, the previous microwave study also found a similar difference in the CC distances within ethyl *tert*-butyl ether, despite fitting all of the heavy atom parameters. The assumed geometric parameters involving the H atoms in the previous work may therefore have been the dominant contribution to the error.

5 Conclusion

A new K_a band CP-FTMW spectrometer has been constructed based on a 150 W TWTA with a careful microwave circuit design to minimize spurious frequencies. Analysis of the chirp power spectrum shows the high spectral purity of the excitation pulse, as well as a gain flatness of 5dB across the 26.5–40 GHz range. It is equipped with a pulsed supersonic expansion source with an optional heated reservoir to allow for measurements of species with low vapor pressures. The performance of the spectrometer has been demonstrated by recording the rotational spectrum of methyl *tert*-butyl ether in the entire 26.5–40 GHz region at multiple temperatures. With the spectral range and coverage, the number of known MTBE transitions has increased from 32 to over 1000, and the first torsionally excited state of the methoxy rotor was identified for the first time. The two states were simultaneously fit to Watson's S-reduced effective Hamiltonian (with quartic and partial sextic centrifugal distortion terms) with a treatment of the internal rotation motion using the $XIAM_{mod}$ program with an overall RMS deviation of below 22 kHz, well below the experimental linewidths. Details of the internal rotation motion were also investigated with ab initio electronic structure calculations. Moreover, the sensitivity of the K_a band spectrometer was sufficient for readily identifying all singly-substituted ^{13}C isotopologues in natural abundance, followed by the ^{18}O isotopologue with the use of the heated reservoir. From the isoptopically substituted spectroscopic constants, an r_0 structure with a complete treatment of the heavy atom positions was carried out, and the results resolve a disagreement in the literature between an earlier microwave-derived structure and a structure derived from electron diffraction measurements. These results highlight the utility of the K_a band range for probing a wide variety of rotational energy levels and serving as a bridge from the sub-cm to the millimeter spectral region.

Author Contributions

KNC–Conceptualization, Methodology, Supervision, Formal Analysis, Data Curation, Writing (original draft). JHW–Investigation, Methodology, Preliminary Analysis, Preliminary Draft. CAD–Investigation, Methodology, Writing (editing). KSM–Investigation, Methodology, Writing (editing). SLJ–Investigation, Methodology, Writing (editing). ZSB–Investigation, Methodology, Writing (editing). PAS–Methodology, Writing (editing).

Conflicts of interest

There are no conflicts to declare.

Acknowledgements

The authors thank the UC Davis Crocker Machine Shop for their invaluable help in the design and fabrication of mechanical components of the K_a band spectrometer, as well as Haley Scolati, Hannah Toru, and Alan Hicklin for contributing to the early design and construction of the spectrometer. The authors also thank P. Bryan Changala and Brian J. Drouin for helpful discussions, John F. Stanton for assistance with the development version of CFOUR, and Alicia O. Hernandez-Castillo for assistance with the B3LYP calculations. Finally, we thank the anonymous referees for their constructive comments. This work has been supported by the NSF grant AST-2042257.

Notes and references

1 G. B. Park and R. W. Field, *J. Chem. Phys.*, 2016, **144**, 200901.
2 G. S. I. Grubbs and S. A. Cooke, *J. Phys. Chem. A*, 2011, **115**, 1086–1091.
3 N. A. Seifert, G. A. Guirgis and B. H. Pate, *J. Mol. Struct.*, 2012, **1023**, 222–226.
4 I. A. Finneran, P. B. Carroll, G. J. Mead and G. A. Blake, *Phys. Chem. Chem. Phys.*, 2016, **18**, 22565–22572.
5 A. Jabri, F. E. Marshall, W. R. N. Tonks, R. E. Brenner, D. J. Gillcrist, C. J. Wurrey, I. Kleiner, G. A. Guirgis and G. S. I. Grubbs, *J. Phys. Chem. A*, 2020, **124**, 3825–3835.
6 D. A. Obenchain, P. Pinacho, S. Zinn and M. Schnell, *J. Mol. Struct.*, 2020, **1213**, 128109.
7 A. K. Huff, N. Love, C. J. Smith and K. R. Leopold, *J. Mol. Spectrosc.*, 2022, **385**, 111623.
8 S. Baweja, E. Antonelli, S. Hussain, A. Fernández-Ramos, I. Kleiner, H. V. L. Nguyen and M. E. Sanz, *Molecules*, 2023, **28**, 2153.
9 S. E. Dutton, E. M. Mastin and G. A. Blake, *Phys. Chem. Chem. Phys.*, 2023, **25**, 5960–5966.
10 X. Chen, G. Wang, X. Zeng, W. Li and M. Zhou, *J. Am. Chem. Soc.*, 2024, **146**, 1484–1490.
11 A. S. Hazrah, A. Insausti, J. Ma, M. H. Al-Jabiri, W. Jäger and Y. Xu, *Angew. Chem. Int. Ed.*, 2023, **62**, e202310610.
12 A. L. Steber, B. Temelso, Z. Kisiel, M. Schnell and C. Pérez, *Proc. Natl. Acad. Sci.*, 2023, **120**, e2214970120.
13 R. M. Gurusinghe, N. Dias, A. M. Mebel and A. G. Suits, *J. Phys. Chem. Lett.*, 2022, **13**, 91–97.
14 O. Chitarra, O. Pirali, J.-T. Spaniol, T. S. Hearne, J.-C. Loison, J. F. Stanton and M.-A. Martin-Drumel, *J. Phys. Chem. A*, 2022, **126**, 7502–7513.
15 K. N. Crabtree, M.-A. Martin-Drumel, G. G. Brown, S. A. Gaster, T. M. Hall and M. C. McCarthy, *J. Chem. Phys.*, 2016, **144**, 124201.
16 M.-A. Martin-Drumel, M. C. McCarthy, D. Patterson, B. A. McGuire and K. N. Crabtree, *J. Chem. Phys.*, 2016, **144**, 124202.
17 M. McCarthy and K. L. K. Lee, *J. Phys. Chem. A*, 2020, **124**,

3002–3017.
18 C. Abeysekera, A. O. Hernandez-Castillo, J. F. Stanton and T. S. Zwier, *J. Phys. Chem. A*, 2018, **122**, 6879–6885.
19 C. Karunatilaka, A. J. Shirar, G. L. Storck, K. M. Hotopp, E. B. Biddle, R. J. Crawley and B. C. Dian, *J. Phys. Chem. Lett.*, 2010, **1**, 1547–1551.
20 N. M. Kidwell, V. Vaquero-Vara, T. K. Ormond, G. T. Buckingham, D. Zhang, D. N. Mehta-Hurt, L. McCaslin, M. R. Nimlos, J. W. Daily, B. C. Dian, J. F. Stanton, G. B. Ellison and T. S. Zwier, *J. Phys. Chem. Lett.*, 2014, **5**, 2201–2207.
21 K. Prozument, Y. V. Suleimanov, B. Buesser, J. M. Oldham, W. H. Green, A. G. Suits and R. W. Field, *J. Phys. Chem. Lett.*, 2014, **5**, 3641–3648.
22 D. P. Zaleski, J. L. Neill, M. T. Muckle, N. A. Seifert, P. Brandon Carroll, S. L. Widicus Weaver and B. H. Pate, *J. Mol. Spectrosc.*, 2012, **280**, 68–76.
23 T. Hua, J. Feng, S. Li and W. Yan, *Int. J. Environ. Sci. Technol.*, 2023, **20**, 11673–11692.
24 I. Levchuk, A. Bhatnagar and M. Sillanpää, *Science of The Total Environment*, 2014, **476–477**, 415–433.
25 M. J. Moran, J. S. Zogorski and P. J. Squillace, *Groundwater*, 2005, **43**, 615–627.
26 R. Suenram, F. Lovas, W. Pereyra, G. Fraser and A. Walker, *J. Mol. Spectrosc.*, 1997, **181**, 67–77.
27 L. N. Gregerson, J. S. Siegel and K. K. Baldridge, *J. Phys. Chem. A*, 2000, **104**, 11106–11110.
28 S. Konaka, H. Takeuchi, K. Siam, J. D. Ewbank and L. Schäfer, *J. Mol. Struct.*, 1990, **222**, 503–508.
29 S. Liedle, H.-G. Mack, H. Oberhammer, M. R. Imam and N. L. Allinger, *J. Mol. Struct.*, 1989, **198**, 1–15.
30 S. Herbers and H. V. L. Nguyen, *J. Mol. Spectrosc.*, 2020, **370**, 111289.
31 Z. Kisiel, *J. Mol. Spectrosc.*, 2003, **218**, 58–67.
32 K. N. Crabtree, *moments.py: v4.1.0, 10.5281/zenodo.8299674*, Zenodo, 2023.
33 Thom H. Dunning, *J. Chem. Phys.*, 1989, **90**, 1007.
34 J. F. Stanton, J. Gauss, L. Cheng, M. E. Harding, D. A. Matthews and P. G. Szalay, *CFOUR, coupled-cluster techniques for computational chemistry, a quantum-chemical program package*.
35 J. F. Stanton and J. Gauss, *Int. Rev. Phys. Chem.*, 2000, **19**, 61–95.
36 P. R. Franke, J. F. Stanton and G. E. Douberly, *J. Phys. Chem. A*, 2021, **125**, 1301–1324.
37 J. Almlöf and P. R. Taylor, *Advances in quantum chemistry*, Academic Press, 1991, vol. 22, pp. 301–373.
38 M. J. Frisch, G. W. Trucks, H. B. Schlegel, G. E. Scuseria, M. A. Robb, J. R. Cheeseman, G. Scalmani, V. Barone, G. A. Petersson, H. Nakatsuji, X. Li, M. Caricato, A. V. Marenich, J. Bloino, B. G. Janesko, R. Gomperts, B. Mennucci, H. P. Hratchian, J. V. Ortiz, A. F. Izmaylov, J. L. Sonnenberg, D. Williams-Young, F. Ding, F. Lipparini, F. Egidi, J. Goings, B. Peng, A. Petrone, T. Henderson, D. Ranasinghe, V. G. Zakrzewski, J. Gao, N. Rega, G. Zheng, W. Liang, M. Hada, M. Ehara, K. Toyota, R. Fukuda, J. Hasegawa, M. Ishida, T. Nakajima, Y. Honda, O. Kitao, H. Nakai, T. Vreven, K. Throssell, J. A. Montgomery, Jr., J. E. Peralta, F. Ogliaro, M. J. Bearpark, J. J. Heyd, E. N. Brothers, K. N. Kudin, V. N. Staroverov, T. A. Keith, R. Kobayashi, J. Normand, K. Raghavachari, A. P. Rendell, J. C. Burant, S. S. Iyengar, J. Tomasi, M. Cossi, J. M. Millam, M. Klene, C. Adamo, R. Cammi, J. W. Ochterski, R. L. Martin, K. Morokuma, O. Farkas, J. B. Foresman and D. J. Fox, *Gaussian~16 Revision C.01*, 2016.
39 R. J. Bartlett, *Coupled-cluster approach to molecular structure and spectra: A step toward predictive quantum chemistry*, 1989.
40 R. J. Bartlett and M. Musiał, *Rev. Mod. Phys.*, 2007, **79**, 291–352.
41 L.-P. Wang and C. Song, *J. Chem. Phys.*, 2016, **144**, 214108.
42 J. R. Durig, S. M. Craven, J. H. Mulligan, C. W. Hawley and J. Bragin, *J. Chem. Phys.*, 1973, **58**, 1281–1291.
43 J. K. G. Watson, *J. Chem. Phys.*, 1967, **46**, 1935–1949.
44 J. H. Carpenter, *J. Mol. Spectrosc.*, 1973, **46**, 348–357.
45 B. P. van Eijck, *J. Mol. Spectrosc.*, 1974, **53**, 246–249.
46 L. Margulès, A. Perrin, J. Demaison, I. Merke, H. Willner, M. Rotger and V. Boudon, *J. Mol. Spectrosc.*, 2009, **256**, 232–237.
47 Y. Zhao, H. V. L. Nguyen, W. Stahl and J. T. Hougen, *J. Mol. Spectrosc.*, 2015, **318**, 91–100.
48 J. Behrend, P. Mittler, G. Winnewisser and K. M. T. Yamada, *J. Mol. Spectrosc.*, 1991, **150**, 99–119.
49 G. Winnewisser, M. Winnewisser and W. Gordy, *J. Chem. Phys.*, 1968, **49**, 3465–3478.
50 G. Winnewisser and P. Helminger, *J. Chem. Phys.*, 1972, **56**, 2967–2979.
51 G. Winnewisser and P. Helminger, *J. Chem. Phys.*, 1972, **56**, 2954–2966.
52 G. Winnewisser, *J. Chem. Phys.*, 1972, **56**, 2944–2954.
53 H. Li, G. S. Ezra and L. A. Philips, *J. Chem. Phys.*, 1992, **97**, 5956–5963.
54 A. Perrin, J. M. Flaud, L. Margulès, J. Demaison, H. Mäder and S. Wörmke, *J. Mol. Spectrosc.*, 2002, **216**, 214–224.
55 A. Perrin, E. Bertseva, J.-M. Flaud, D. Collet, H. Bürger, T. Masiello and T. A. Blake, *Mol. Phys.*, 2007, **105**, 1833–1848.
56 L. H. Coudert and A. Perrin, *J. Mol. Spectrosc.*, 1995, **172**, 352–368.
57 J. Pyka and N. Ohashi, *J. Mol. Spectrosc.*, 2001, **207**, 83–88.